Supporting Information: Engineering the Electronic and Thermal Properties of Two-Dimensional Covalent Organic Frameworks

Muhammad Akif Rahman,[†] Sandip Thakur,[†] Patrick E. Hopkins,[‡] and Ashutosh Giri[*,†]

†*Department of Mechanical Industrial and Systems Engineering, University of Rhode Island, Kingston, RI 02881, United States*

‡*Department of Mechanical and Aerospace Engineering, University of Virginia, Charlottesville, 559 Virginia 22904, United States*

E-mail: ashgiri@uri.edu

Arylene-ethynylene Macrocycle

(AEM-COF1)

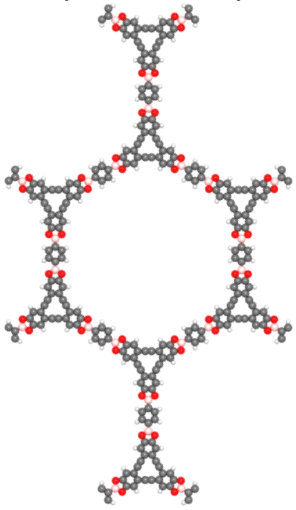

$(C_{66}H_{40}B_6O_{12})$

Imine-based

(COF-LZU1)

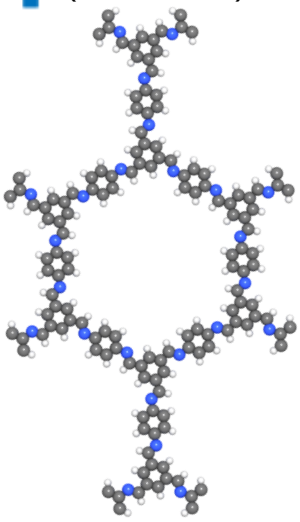

$(C_{36}H_{36}N_6)$

Boroxine anhydride

(COF-1)

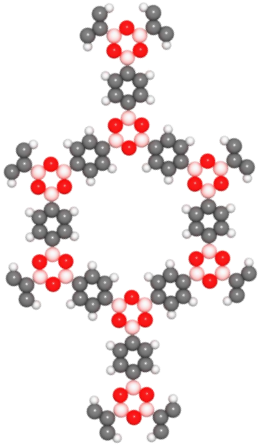

$(C_{18}H_{38}B_6O_6)$

C
H
B
N
O
S

Boronate-ester

(COF-8)

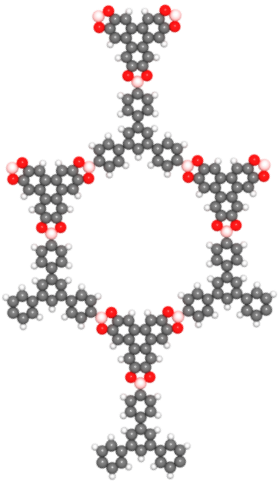

$(C_{42}H_{25}B_3O_6)$

Boron-triazine

(BTA-COF1)

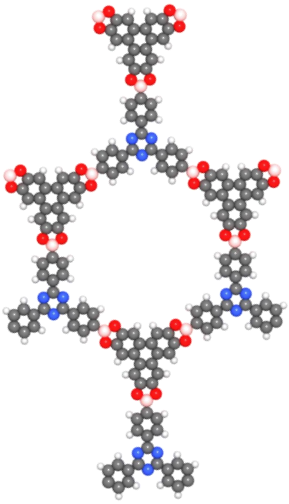

$(C_{39}H_{22}B_3N_3O_6)$

Borazine-linked polymer

(BLP-2H)

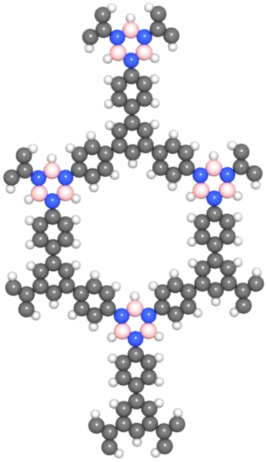

$(C_{24}H_{30}B_3N_3)$

Boronate-ester

(COF-6)

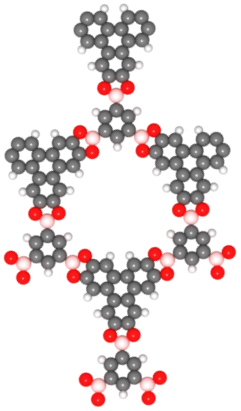

$(C_{24}H_{17}B_3O_6)$

Covalent triazine framework

(CTF-1)

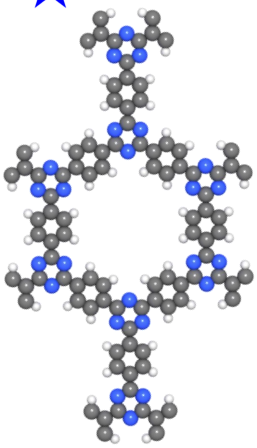

$(C_{24}H_{24}N_6)$

Boron-triazine

(BTA-COF4)

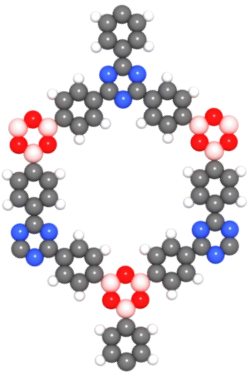

$(C_{21}H_{20}B_3N_3O_3)$

Benzotrithiophene diaminodiphenyl

(BTT-DADP)

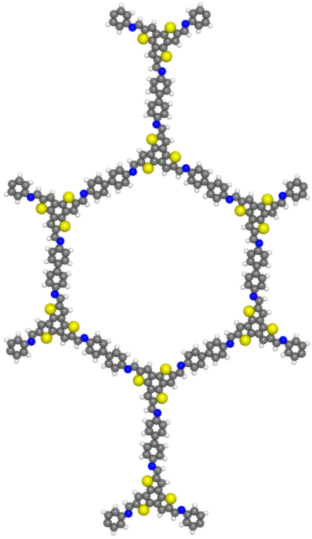

$(C_{66}H_{40}N_6S_6)$

Imine-based

(N3-COF)

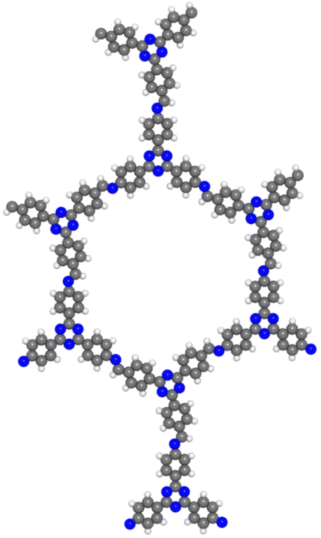

$(C_{45}H_{35}N_9)$

Benzotrithiophene diaminobenzene

(BTT-TAB)

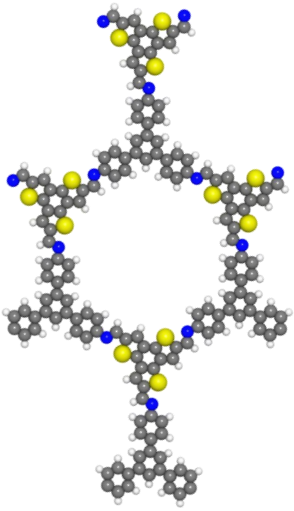

$(C_{39}H_{25}N_3S_3)$

β-ketoenamine-linked
Triformylphloroglucinol

(CCOF-TpBD)

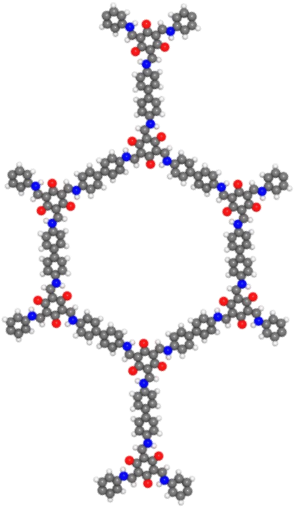

$(C_{54}H_{46}N_6O_6)$

Benzotrithiophene
diaminodiphenyl

(BTT-DAB)

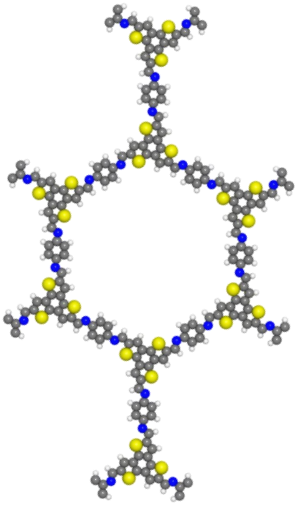

$(C_{48}H_{36}N_6S_6)$

β-ketoenamine-linked
Triformylphloroglucinol

(CCOF-TpPa)

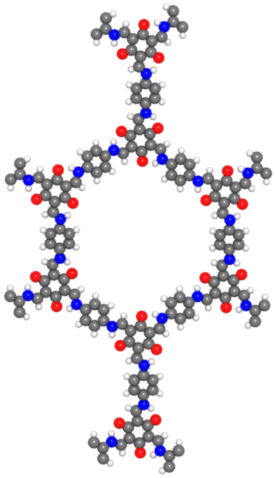

$(C_{36}H_{42}N_6O_6)$

Azine-based

(ACOF-1)

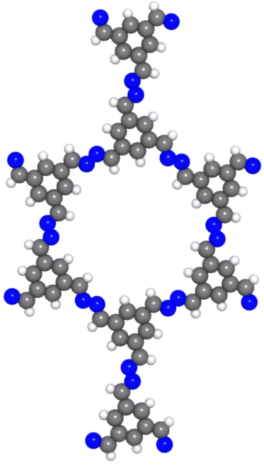

$(C_{18}H_{24}N_6)$

Azine-based
(COF-JLU2)

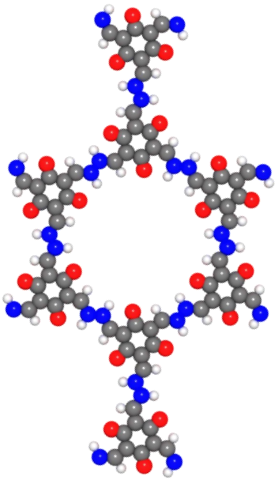

$(C_{18}H_{16}N_6O_6)$

Benzo-bis(oxazole)

(BBO-COF1)

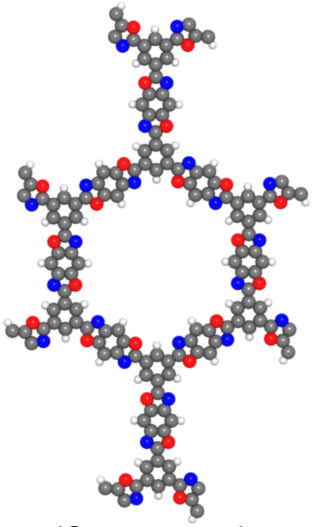

$(C_{36}H_{24}N_6O_6)$

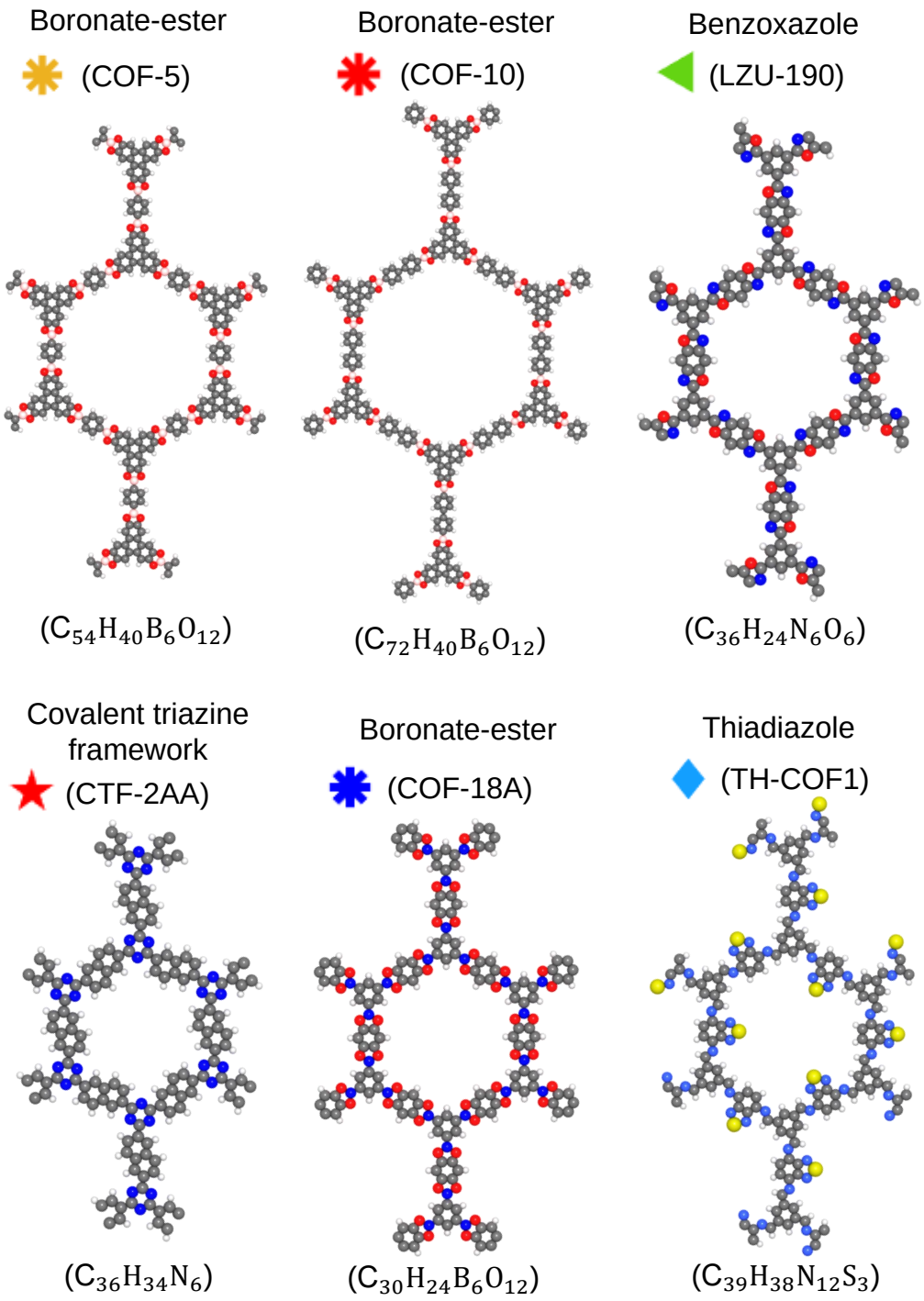

Figure S1: Schematic illustration of our 2D COF molecular structures.

Figure S1 shows the schematic representation of molecular structures for our 2D COFs. In our study, we calculate the electronic properties of these 2D COFs with hexagonal topologies, which have been experimentally synthesized.[1]

I. Density Functional Theory (DFT) Calculation

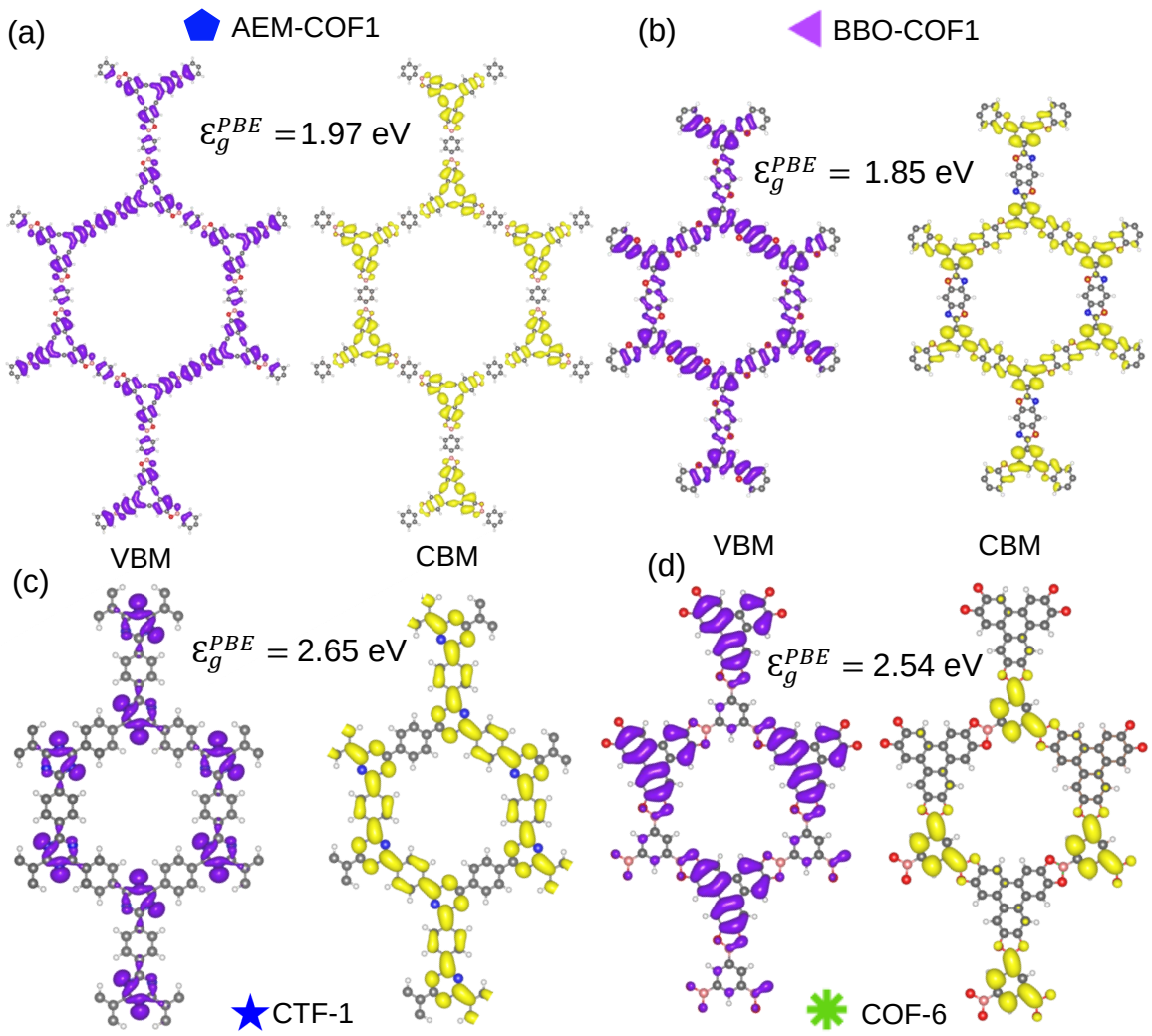

Figure S2: Spatial distribution of charge densities of VBM (purple isosurface) and CBM (yellow isosurface) for (a) AEM-COF1, (b) BBO-COF1, (c) CTF-1, and (d) COF-6 structures. COFs with lower electronic band gaps (AEM-COF1 and BBO-COF1 structures) exhibit delocalized charge densities resulting in larger spatial overlaps between the VBM and CBM. Whereas, CTF-1 and COF-6 structures (having relatively higher electronic band gaps) show localized charge densities without considerable spatial overlap of the VBM and CBM.

To investigate the differences in the electronic localization functions of our 2D COF structures, we calculate the charge densities of the Valence Band Maximum (VBM) and the Conduction Band Minimum (CBM). For both the AEM-COF1 and BBO-COF1 structures with relatively lower electronic band gaps, we observe delocalized charge distribution of both the VBM and CBM as shown

in Figs. S2a and S2b resulting in considerable spatial overlap between the VBM and the CBM. In contrast, for both the CTF-1 and COF-6 structures with relatively higher electronic band gaps, we see more confined charge densities as shown in Figs. S2c and S2d. This difference in spatial distribution of charge densities suggests that the electronic band gap of COF structures increases with the increase in charge localization.

II. Molecular Dynamics (MD) Simulations

A. Equilibrium MD (EMD) Simulation

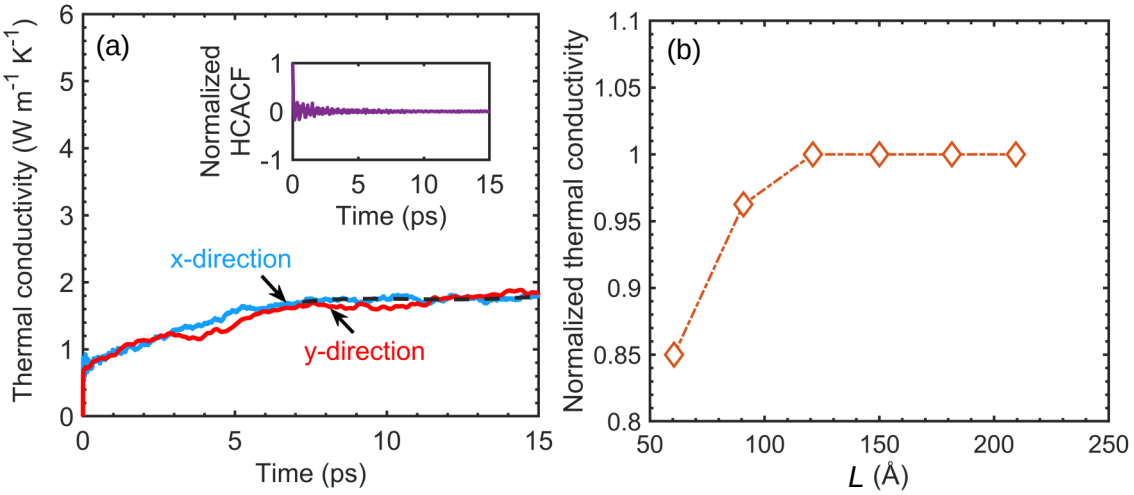

Figure S3: (a) Green-Kubo predicted thermal conductivity of our monolayer 2D COF-5 structure using the AIREBO potential at 300 K in the x- and y-direction as a function of the integration time, showing same thermal conductivities in both directions. (inset) A fully decayed normalized heat current autocorrelation function (HCACF) as a function of the integration time. (b) Normalized thermal conductivity of COF-5 with respect to thermal conductivity of the 12 nm COF-5 domain as a function of computational domain length in the x-direction. A domain length greater than $L \sim$120.1 Å is enough to avoid any size effects in our results.

We use the total correlation time period of 15 ps to achieve converged HCACF, as shown in the insets of Fig. S3a and Fig. S4a. Furthermore, we use the sampling interval of 10 fs during the data collection period to calculate the heat current autocorrelation function across the entire

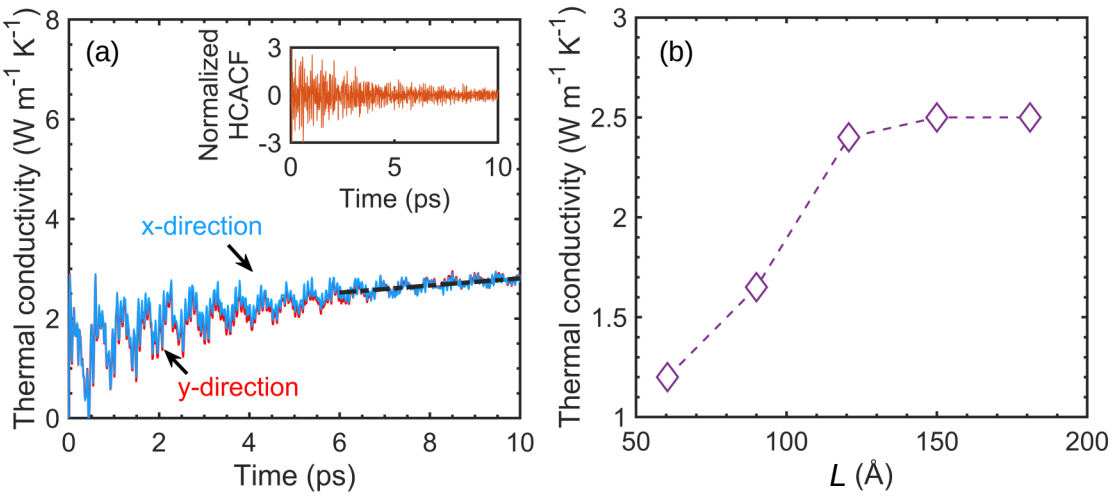

Figure S4: (a) Green-Kubo predicted thermal conductivity of our 2D COF-5 structure utilizing the UFF potential at 300 K in the x- and y-directions as a function of the integration time, showing same thermal conductivities in both directions. (inset) A fully decayed normalized heat current autocorrelation function (HCACF) as a function of the integration time. (b) Thermal conductivity of our 2D monolayer COF-5 as described by the UFF potential a function of computational domain length in the x-direction. A domain length greater than $L \sim$120.1 Å is enough to avoid any size effects in our results.

temperature range followed by integration of the heat current autocorrelation function to predict the converged thermal conductivity for our 2D COF structures.

Figure S3a and Figure S4a show the converged thermal conductivity for our COF-5 structure at 300 K, which is calculated by the integration of the heat current from 7 ps to 15 ps and 6 ps to 10 ps when utilizing the AIREBO and UFF potentials, respectively. We ensure that our results are not influenced by the choice of our computational domain size across the whole temperature range by conducting a series of MD simulations with varying simulation domain sizes from $\sim$60 Å to $\sim$210 Å as shown in Fig. S3b and Fig. S4b. The convergence of thermal conductivity within uncertainties for computational domain lengths greater than $\sim$120.1 Å ensures that our choice of the domain size does not influence our GK predictions.

B. Non-equilibrium MD (NEMD) simulation

To further support our results obtained from the GK formalism under the EMD simulations framework, we perform additional non-equilibrium molecular dynamics (NEMD) simulations to validate the thermal conductivity of our COF-5 structure using the LAMMPS package.[2] In this approach, we prescribe hot and cold baths at opposite ends of the simulation domain to create steady-state temperature profiles from which we predict the thermal conductivity by invoking the Fourier's law as shown in Fig. S5 for our COF-5 computational domain.

After we obtain a steady-state temperature profile, the thermal conductivity is calculated as,

$$\dot{Q} = -\kappa \frac{dT}{dx}. \tag{1}$$

where $\dot{Q}$ is the rate of heat flux added and subtracted from the hot and cold regions, κ is the thermal conductivity, and $\frac{dT}{dx}$ is the temperature gradient averaged over time and space.

To account for the effect of computational domain size (i.e. scattering of long wavelength phonons near and at the heat source/sink region),[3–5] we extrapolated the thermal conductivity value to the limit of an infinite system length (i.e. $\kappa_{L\to\infty}$). The inverse thermal conductivity and inverse system length is related by the following equation (Eq. 4) when the length of the system is comparable or larger than the average phonon mean free path (λ):

$$\frac{1}{\kappa(L)} = \frac{1}{\kappa_{L\to\infty}} \left(1 + \frac{\lambda}{L}\right). \tag{2}$$

Figure S5b shows an example of the temperature profile for a computational domain of the COF-5 structure obtained with the NEMD approach where a heat flux is applied in the in-plane direction. To predict the 'bulk' thermal conductivity of our COF-5 structure, we plot the inverse of κ as a function of the inverse of the computational domain length (L) in the direction of heat flux applied as shown in Fig. S5c and extrapolated the linear fits to $1/L \to 0$ to extract the 'bulk' thermal conductivity.

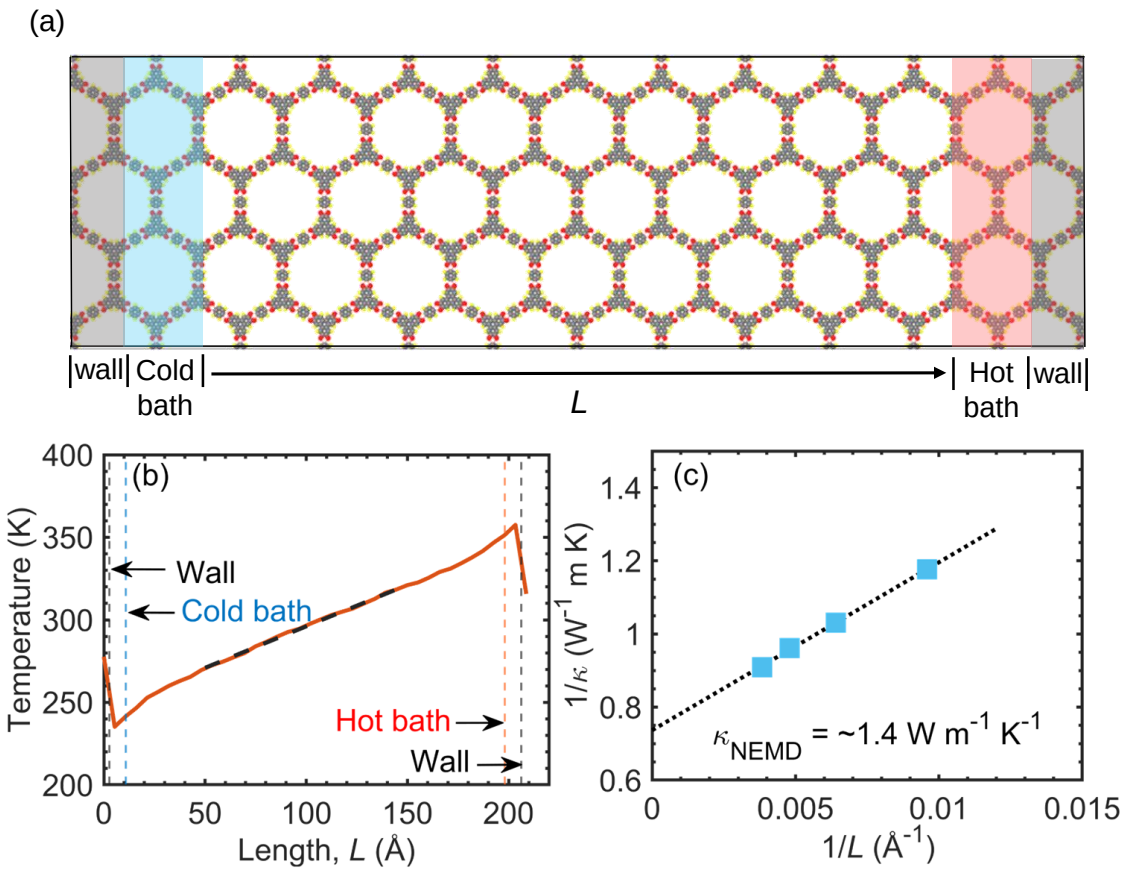

Figure S5: (a) Schematic illustration of the computational domain for our 2D COF-5 structure used in our NEMD simulations to predict the in-plane thermal conductivities. (b) Steady-state temperature profile in the x-direction, which we utilize to predict the thermal conductivity by invoking the Fourier's law of heat conduction. (c) Inverse of the NEMD-predicted size-dependent thermal conductivity for COF-5 structure as a function of the inverse of the computational domain length along the direction of applied heat. The 'bulk' thermal conductivity is predicted by extrapolating the linear fits to $1/L \rightarrow 0$.

Similar to our GK-predicted thermal conductivity, we calculate 'bulk' thermal conductivity of $\sim$1.4 Wm^{-1}K^{-1} for the COF-5 structure in the in-plane direction using our NEMD simulations.

C. Phonon Spectral Energy Density (SED) Calculation

Figures S6c and S6d show the SEDs at 300 K for short-COF-5 and CCOF-TpPa structures having similar mass densities but with varying node sizes. We observe resolved and less broadened peaks in the short-COF-5 structure (with larger nodes) as compared to the CCOF-TpPa structure (with

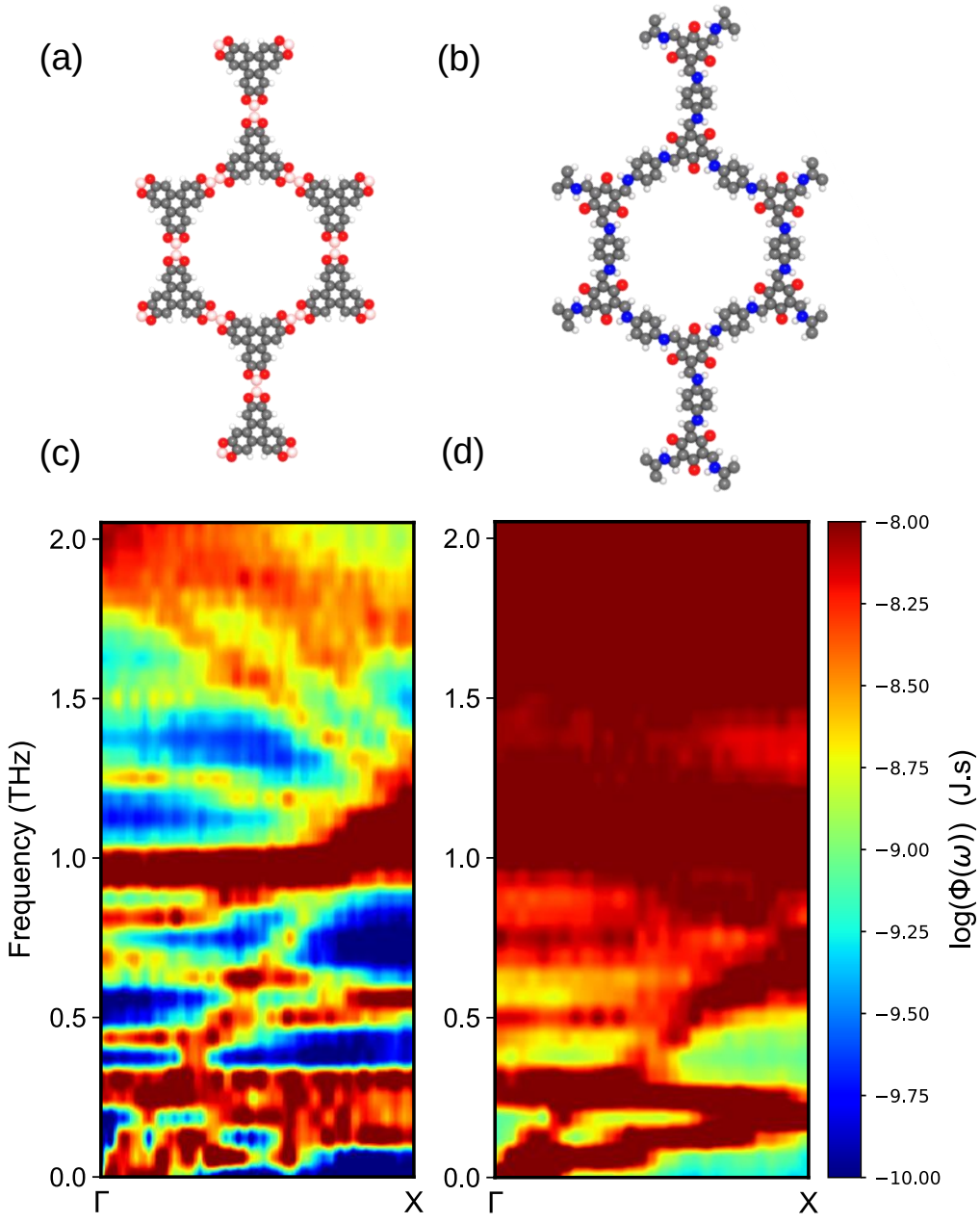

Figure S6: Schematic illustration of molecular structures of (a) short-COF-5 (modified COF-5 structure without benzene linker) and (b) CCOF-TpPa. Calculated phonon spectral energy densities for (c) short-COF-5 and (d) CCOF-TpPa structures at 300 K. The relatively resolved and sharp peaks in the short-COF-5 structure show less anharmonicity and weak coupling between the acoustic modes and the optic modes as compared to the strongly anharmonic CCOF-TpPa structure.

relatively smaller nodes) which suggests that the bigger nodes are associated with lower anharmonicities and weak coupling between the acoustic modes and the optic modes. This results in the

relatively higher thermal conductivity for the COFs with bigger nodes as compared to the COFs with smaller nodes but having similar mass densities (see Fig. 4 of the main paper).

D. Vibrational Density of States Calculations

To analyze the vibrational density of states (vDOS) of our COF structures with different densities, we output the velocity of each atom of the COF structures every 10 time steps for a total of 1 ns to obtain a velocity fluctuation time series. We perform fourier transformation of the velocity autocorrelation function (VACF) by implementing the Welch method of power spectral density which is given as,

$$D(\omega) = \frac{1}{2} m \mathcal{F}(VACF) \frac{1}{k_{\mathrm{B}} T} \rho. \tag{3}$$

where m, k_{B}, T, and ρ are the mass of individual atoms, Boltzmann constant, temperature, and atomic density of the computational domain, respectively.

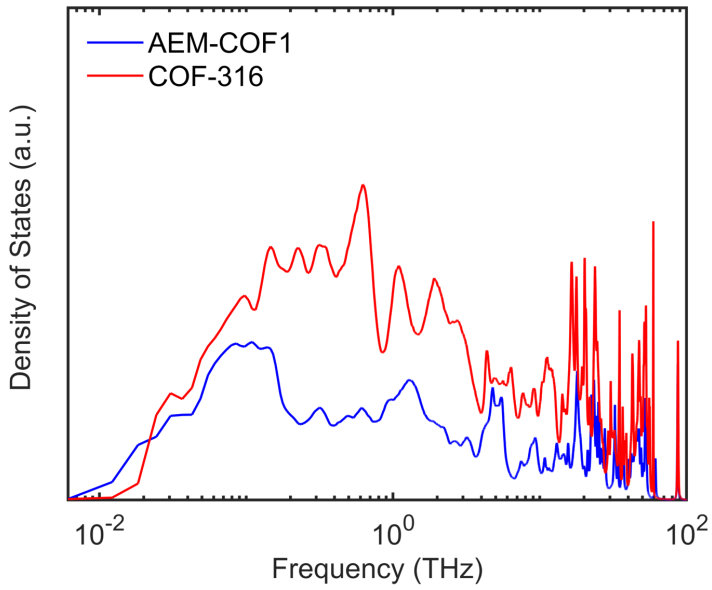

Figure S7: Comparison of vibrational density of states for AEM-COF1 (0.47 g cm^{-3}) and COF-316 (1.14 g cm^{-3}) structures. The vibrational densities increases throughout the vibrational spectrum for COF-316 structure as compared to AEM-COF1 structure with relatively lower mass density.

We compare the vDOS of AEM-COF1 structure having mass density of 0.47 g cm^{-3} with

COF-316 structure having relatively higher mass density of 1.14 g cm^{-3} as shown in Figure S7. We see considerable increase in the vibrational densities throughout the vibrational spectrum for COF-316 structure as compared to AEM-COF1 structure with relatively lower mass density which suggests that these additional increase in vibrational densities across all the frequency range might be providing the additional channels of heat transfer resulting in the higher thermal conductivitity for the structures with relatively higher mass densities.

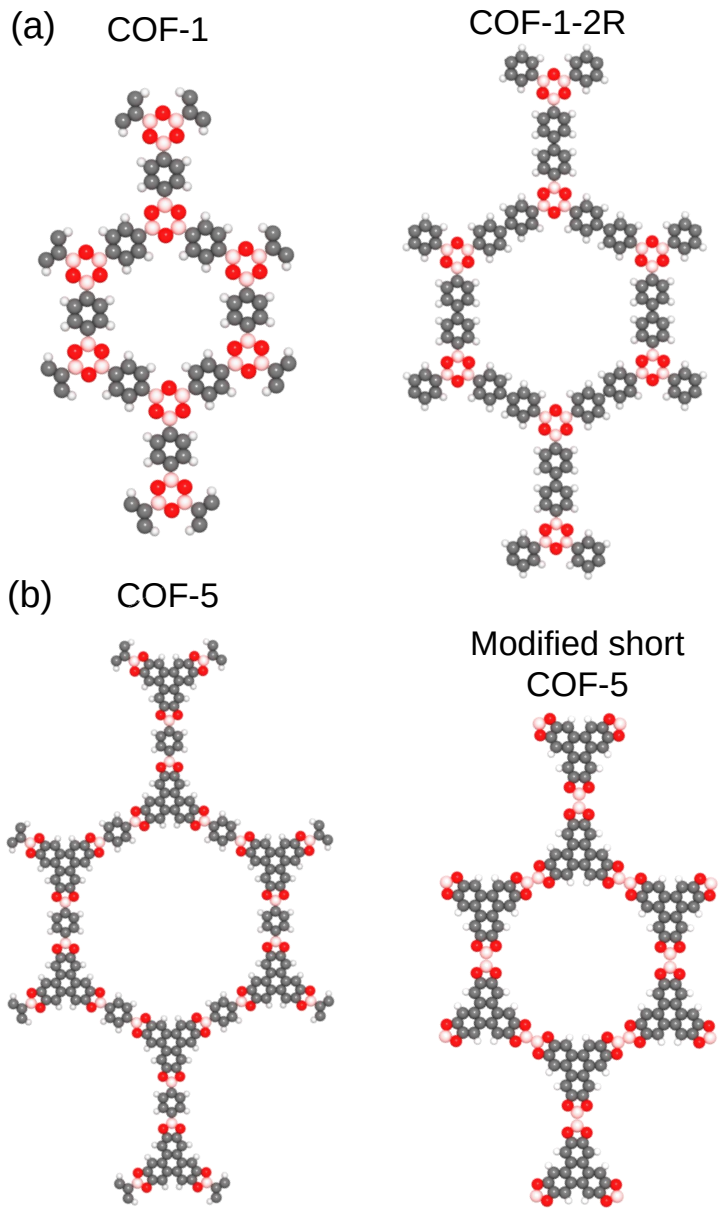

Figure S8: Schematic illustration of molecular structures of (a) COF-1 and COF-1-2R (represented by hollow circle symbols in Fig. 4 of the main manuscript). Schematic illustration of molecular structures of (b) COF-5 and modified short COF-5 (represented by hollow triangle symbols in Fig. 4 of the main manuscript). For both COF families, the thermal conductivity decreases monotonically with the increase in linker length albeit having 2 different node types.

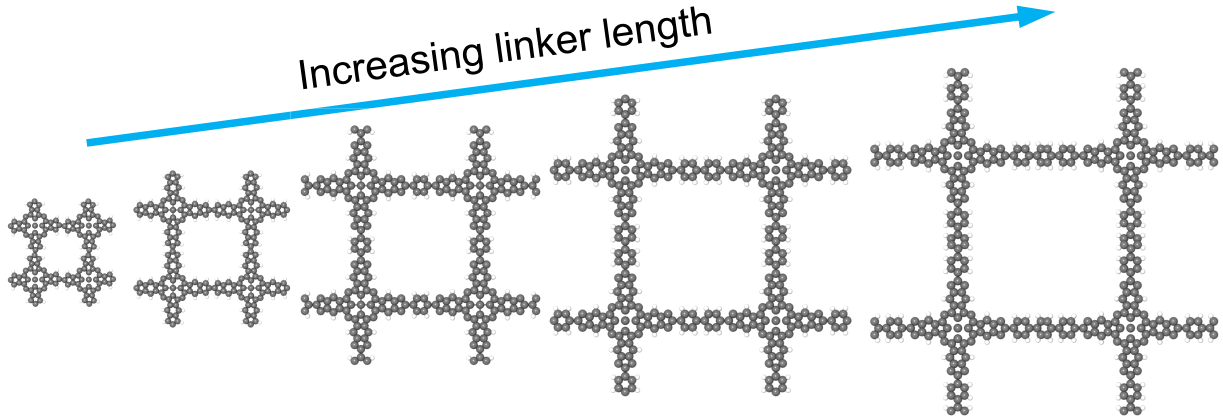

Figure S9: Schematic illustration of the molecular structures of our square pore COF with increasing linker length (from left to right). The thermal conductivity monotonically decreases with the increasing linker lengths (decreasing mass densities) as shown by hollow square symbols in Fig. 4 of the main manuscript.

References

(1) Wang, Y.; Wang, G.; Liu, Y.; Zheng, B.; Wang, Z.; Yang, Q. Identifying promising covalent-organic frameworks for decarburization and desulfurization from biogas via computational screening. *ACS Sustainable Chemistry & Engineering* **2021**, *9*, 8858–8867.

(2) Plimpton, S. Fast parallel algorithms for short-range molecular dynamics. *Journal of computational physics* **1995**, *117*, 1–19.

(3) Schelling, P. K.; Phillpot, S. R.; Keblinski, P. Comparison of atomic-level simulation methods for computing thermal conductivity. *Physical Review B* **2002**, *65*, 144306.

(4) Tang, Q. A molecular dynamics simulation: the effect of finite size on the thermal conductivity in a single crystal silicon. *Molecular Physics* **2004**, *102*, 1959–1964.

(5) Jund, P.; Jullien, R. Molecular-dynamics calculation of the thermal conductivity of vitreous silica. *Physical review B* **1999**, *59*, 13707.